1-D numerical modelling of shallow flows with variable horizontal density

Feifei Zhang Leighton[*,†,‡], Alistair G. L. Borthwick and Paul H. Taylor

Department of Engineering Science, University of Oxford, Oxford OX1 3PJ, U.K.

SUMMARY

A 1-D numerical model is presented for vertically homogeneous shallow flows with variable horizontal density. The governing equations represent depth-averaged mass and momentum conservation of a liquid–species mixture, and mass conservation of the species in the horizontal direction. Here, the term 'species' refers to material transported with the liquid flow. For example, when the species is taken to be suspended sediment, the model provides an idealized simulation of hyper-concentrated sediment-laden flows. The volumetric species concentration acts as an active scalar, allowing the species dynamics to modify the flow structure. A Godunov-type finite volume scheme is implemented to solve the conservation laws written in a deviatoric, hyperbolic form. The model is verified for variable-density flows, where analytical steady-state solutions are derived. The agreement between the numerical predictions and benchmark test solutions illustrates the ability of the model to capture rapidly varying flow features over uniform and non-uniform bed topography. A parameter study examines the effects of varying the initial density and depth in different regions. Copyright © 2009 John Wiley & Sons, Ltd.

1. INTRODUCTION

Species transport processes in shallow flows may be modelled using either a single-phase or a multi-phase approach depending on whether the mixtures can be considered homogeneous. For non-homogeneous mixtures with large gradients of concentration in the vertical direction,

---

[*]Correspondence to: Feifei Zhang Leighton, Department of Engineering Science, University of Oxford, Oxford OX1 3PJ, U.K.
[†]E-mail: LeightonF@halcrow.com
[‡]Current address: Halcrow Group Ltd, Burderop Park, Swindon SN4 0QD, U.K.

two-phase models are used to treat separately the solid and liquid phases in order to simulate morphological evolution and stratified flows (see e.g. [1, 2]). Owing to the complexity of the interaction between fluid and solid particles, a typical two-phase model consists of six governing equations plus complicated boundary and interface conditions at the fluid–sediment interface.

In most rivers and streams, fully turbulent conditions achieve rapid vertical mixing and it can be appropriate to assume the mixture to be vertically well mixed. It is then possible to consider the mixture to be homogeneous and single phase in situations where no significant morphological changes occur [3]. Several single-phase shallow flow and species transport models have been developed, where the non-linear shallow water and species transport equations are solved simultaneously using a coupled approach (e.g. [4–6]). The majority of these models treat the species as a passive scalar (i.e. a quantity that is passively advected with the fluid). The mass and momentum equations may then be simplified by assuming density to be a constant. This assumption applies to dilute flows containing low species concentrations. However in many practical applications, such as hyper-concentrated sediment transport and debris flows, the species concentration reaches such a high value that the species changes from passive to active. In such cases, the presence of large quantities of material alters the mechanical properties of the liquid–species mixture from those of a pure liquid. A density-dependent hydrodynamic model is thus necessary to describe the behaviour of the liquid–species mixture. Cao *et al.* [7, 8] have developed such a model for simulating hyper-concentrated sediment-laden flow, which has been applied to dam-break flow over an erodible bed and sediment-laden floods in the Yellow River. Recently, Takahashi [9] has provided a comprehensive review of debris flow modelling strategies.

The aim of the present paper is to describe a 1-D numerical model that simulates the transport of vertically homogeneous liquid–species mixtures in shallow flows, where sharp depth and horizontal density gradients may occur locally. Section 2 presents a derivation of the coupled variable-density non-linear shallow flow and species transport equations in hyperbolic conservation form. By considering the liquid–species mixture to be homogeneous in the vertical direction, the conservation laws obtained for the mixture can be expressed in depth-averaged form, similar to those derived by Abbott [10] among others for vertically homogeneous fluids. Section 3 describes the Godunov-type numerical scheme used to solve the variable-density non-linear shallow flow and species transport equations in equilibrium-corrected form. Section 4 presents numerical model validation for variable density shallow cases with analytical steady-state solutions, and 1-D dam-break analogues with one or two initial discontinuities in density. The main conclusions are listed in Section 5.

2. MATHEMATICAL FORMULATION

Let us consider an infinitesimal element located at x of horizontal extent dx through which a shallow flow passes with depth-integrated velocity component in the x-direction $u(x, t)$ and depth $h(x, t)$, where t is time. We assume that the flow is almost horizontal, the vertical component of acceleration is vanishingly small, the pressure can be taken to be hydrostatic, the free surface gravity waves are long with respect to the mean flow depth and wave amplitude, and the liquid–species mixture is vertically homogeneous and non-reactive. Let ρ be the depth-averaged density of the liquid–species mixture and c the non-dimensional depth-averaged species concentration by volume. By taking an infinitesimal time interval dt, the following fundamental conservation laws (see e.g. [10]) are obtained by balancing the net inflow of mass, momentum and species through the boundaries of the control volume while accounting for the accumulation of mass, resultant

forces and species within the control volume. The possibility of relative motion (slip) between the components of the fluid mixture is discounted.

Mass conservation of the mixture:

$$\frac{\partial(\rho h)}{\partial t} + \frac{\partial(\rho u h)}{\partial x} = 0 \qquad (1)$$

Momentum flux balance in the x-direction

$$\frac{\partial(\rho u h)}{\partial t} + \frac{\partial(\rho u^2 h + \frac{1}{2}\rho g h^2)}{\partial x} = \tau_w - \tau_b - \rho g h S_o + \frac{\partial(hT)}{\partial x} \qquad (2)$$

where g is the acceleration due to gravity, τ_w is the tangential surface stress component, τ_b is the bed shear stress, S_o is the bed slope, and T is the effective stress due to viscous effects.

Species mass conservation

$$\frac{\partial(\rho_s c h)}{\partial t} + \frac{\partial(\rho_s u c h)}{\partial x} = \frac{\partial}{\partial x}\left(K h \frac{\partial(\rho_s c)}{\partial x}\right) \qquad (3)$$

where K is the longitudinal mixing coefficient and ρ_s is the density of the species (e.g. density of suspended sediment in a hyper-concentrated flow).

It should be noted that Equations (2) and (3) contain surface, bed, and internal effective stresses, and mixing terms for completeness. However, in the numerical examples given in this paper, we neglect these terms in order to demonstrate the resolution of sharp depth and density fronts by the shock-capturing scheme.

Equation (3) is used to model the dispersion process of the species, which consists of differential advection and horizontal mixing. The density of the liquid–species mixture, ρ, is defined as

$$\rho = \rho_w + c(\rho_s - \rho_w) \qquad (4)$$

where ρ_w is the density of the liquid and ρ_s is the density of the species. The species can be a solid or another liquid so the mixture is either a solid–liquid mixture (e.g. suspended sediment in water) or a binary liquid mixture. For clarity, the liquid with density ρ_w will be referred to as the (ambient) liquid and the liquid or solid with density ρ_s will be denoted as the species. Equivalently, the volumetric concentration c can be expressed in terms of ρ_w, ρ_s, and ρ as

$$c = \frac{\rho - \rho_w}{\rho_s - \rho_w} \quad \text{if } \rho_s \neq \rho_w \qquad (5)$$

Therefore, the variables ρ and c are coupled, and if one of the variables is known then the value of the other can be determined using (4) or (5). For simplicity, the density is expressed as a function of the volumetric concentration in this paper. Another advantage of choosing concentration over density to represent the transport process is that the role of variable c switches from an active scalar to a passive scalar when $\rho = $ constant and $c \neq 0$. Under such conditions, the governing equations reduce to the classical shallow water equations and separate de-coupled species transport equation.

The conservation laws (1)–(3) can be expressed as a hyperbolic system of partial differential equations in the following vector form:

$$\frac{\partial \mathbf{q}}{\partial t} + \frac{\partial \mathbf{f}}{\partial x} = \mathbf{h} \qquad (6)$$

where the vector of the conserved variables $\mathbf{q}$, the flux vector $\mathbf{f}(\mathbf{q})$ and the source terms vector $\mathbf{h}(\mathbf{q})$ are

$$\mathbf{q} = \begin{bmatrix} \rho h \\ \rho u h \\ \rho_s c h \end{bmatrix}, \quad \mathbf{f} = \begin{bmatrix} \rho u h \\ \rho u^2 h + \dfrac{1}{2}\rho g h^2 \\ \rho_s u c h \end{bmatrix} \quad \text{and} \quad \mathbf{h} = \begin{bmatrix} 0 \\ \tau_w - \tau_b - \rho g h S_o + \dfrac{\partial(hT)}{\partial x} \\ \dfrac{\partial}{\partial x}\left(K h \dfrac{\partial(\rho_s c)}{\partial x} \right) \end{bmatrix} \tag{7}$$

The bed shear stress τ_b is approximated by a quadratic friction law

$$\tau_w = \rho C_f u|u| \tag{8}$$

where C_f is an empirical bed friction coefficient. The bed slope S_o is the gradient of the bed profile $z_b(x)$ above an arbitrary datum

$$S_o = \frac{\partial z_b}{\partial x} \tag{9}$$

The effective stress is approximated by

$$T = 2\rho\varepsilon\frac{\partial u}{\partial x} \tag{10}$$

in which ε is the kinematic eddy viscosity coefficient and u is the mean (and slowly varying) horizontal velocity.

By applying the generalized flux gradient and source term balancing technique proposed by Rogers *et al.* [11], the hyperbolic system of conservation laws in (6) is transformed to

$$\frac{\partial\tilde{\mathbf{q}}}{\partial t} + \frac{\partial\tilde{\mathbf{f}}}{\partial x} = \tilde{\mathbf{h}} \tag{11}$$

where $\tilde{\mathbf{q}} = \mathbf{q} - \mathbf{q}^{\text{eq}}$ is the equilibrium-corrected vector of conserved variables, $\tilde{\mathbf{f}} = \mathbf{f}(\mathbf{q}) - \mathbf{f}(\mathbf{q}^{\text{eq}})$ is the equilibrium-corrected flux vector, and $\tilde{\mathbf{h}} = \mathbf{h}(\mathbf{q}) - \mathbf{h}(\mathbf{q}^{\text{eq}})$ is the equilibrium-corrected source term vector. This guarantees the elimination of any problems associated with non-physical apparently unbalanced flux gradient and source terms, while preserving the hyperbolicity of the original equations, and is independent of the order of the numerical approximation [11]. For a flow in a domain Ω with boundary S, the hyperbolic system of conservation equations in vector form (11) can be written in integral form as:

$$\frac{\partial}{\partial t}\int_\Omega \tilde{\mathbf{q}}\,\mathrm{d}\Omega + \int_\Omega \frac{\partial\tilde{\mathbf{f}}}{\partial x}\,\mathrm{d}\Omega = \int_\Omega \tilde{\mathbf{h}}\,\mathrm{d}\Omega \tag{12}$$

Applying Gauss' theorem to the second term gives

$$\frac{\partial}{\partial t}\int_\Omega \tilde{\mathbf{q}}\,\mathrm{d}\Omega + \int_S \tilde{\mathbf{f}}\,\mathrm{d}S = \int_\Omega \tilde{\mathbf{h}}\,\mathrm{d}\Omega \tag{13}$$

where S is the surface through which the net flux passes. The equilibrium-corrected vectors of the conserved variables, fluxes, and source terms are given by:

$$\tilde{\mathbf{q}} = \begin{bmatrix} \rho h - \rho^{\text{eq}} h^{\text{eq}} \\ \rho u h \\ \rho_s c h - \rho_s c^{\text{eq}} h^{\text{eq}} \end{bmatrix}, \quad \tilde{\mathbf{f}} = \begin{bmatrix} \rho u h \\ \rho u^2 h + \dfrac{1}{2}\rho g h^2 - \dfrac{1}{2}\rho^{\text{eq}} g h^{\text{eq}^2} \\ \rho_s u c h \end{bmatrix}$$

and

$$\tilde{\mathbf{h}} = \begin{bmatrix} 0 \\ \tau_w - \tau_b - \rho g h S_o + \rho^{\text{eq}} g h^{\text{eq}} S_o + \dfrac{\partial(hT)}{\partial x} \\ \dfrac{\partial}{\partial x}\left(K h \dfrac{\partial(\rho_s c)}{\partial x} \right) \end{bmatrix} \tag{14}$$

When defining the equilibrium for the system prior to the simulation, it is generally convenient to choose the quiescent state equilibrium of pure liquid defined as: $u^{\text{eq}} = 0$, $\rho^{\text{eq}} = \rho_w$, $c^{\text{eq}} = 0$, and $h^{\text{eq}} = h_s$, where h_s is the mean liquid depth given by

$$h_s(x) = \frac{1}{L}\int_0^L [h(x) + z_b(x)]\,\mathrm{d}x - z_b(x) \tag{15}$$

in which $z_b(x)$ is the bed profile, $h(x)$ is the local total depth of liquid, and the domain occupies the region $0 \leqslant x \leqslant L$. Another equilibrium state is the steady-state equilibrium defined by $u^{\text{eq}} = \text{constant}$ and $\partial \mathbf{q}/\partial t = \mathbf{0}$. The steady-state flow equilibrium may be difficult to evaluate *a priori* because the calculation requires solving a system of ordinary differential equations for spatial variation.

Unlike the above coupled equilibrium-corrected variable-density shallow flow and species transport equations, the conventional non-linear shallow water equations and species transport equation are limited by the assumption that the species is of such a low concentration that the transport process does not affect the flow. This assumption becomes unrealistic for large values of species concentration, which influences the flow velocity. Even at low concentration, a discontinuity in the concentration can affect the flow whereby the higher density region will try to balance the lower density region. This is an analogue to the dam-break problem (with a discontinuity in water depth) that can lead to contact discontinuities, rarefactions and shock waves.

In the variable-density shallow flow and species transport equations, the variables h, u, c, and ρ are solved in a fully coupled manner. The role of the volumetric concentration c is an active scalar so any variation of species concentration occurs with simultaneous variation of the depth, density and flow velocity.

The conventional shallow water and species transport equations are simplifications of the variable-density shallow flow and species transport equations for constant density cases with non-zero species concentration. In this case, the variable c has changed its role from active to passive. This can be shown by taking $\rho = \rho^{\text{eq}}$ and $c^{\text{eq}} = 0$ in (14) and dividing each equation by the common

density constant. By expressing the deviated depth $h - h^{\mathrm{eq}}$ as the free surface elevation η, the following vector expressions are obtained:

$$\tilde{\mathbf{q}} = \begin{bmatrix} \eta \\ uh \\ ch \end{bmatrix}, \quad \tilde{\mathbf{f}} = \begin{bmatrix} uh \\ u^2 h + \dfrac{1}{2} g (\eta^2 + 2\eta h_s) \\ uch \end{bmatrix}$$

and

$$\tilde{\mathbf{h}} = \begin{bmatrix} 0 \\ \dfrac{(\tau_w - \tau_b)}{\rho} - g\eta S_o + \dfrac{1}{\rho} \dfrac{\partial (hT)}{\partial x} \\ \dfrac{\partial}{\partial x} \left(Kh \dfrac{\partial (\rho_s c)}{\partial x} \right) \end{bmatrix} \tag{16}$$

The above equations are essentially the de-coupled 1-D non-linear shallow water and species transport equations. This indicates that the model has a wide range of applicability in that the new variable-density shallow flow and species transport equations transform to the conventional non-linear shallow water equations plus the advection–diffusion equation for species transport when $\rho = \mathrm{constant}$ and $c \neq 0$.

In the absence of any source or sink, volume conservation results from mass conservation of both the mixture and the species. If the bed friction, wind stress, Coriolis parameter, viscosity and diffusivity are all set to zero so that there is no loss or gain of energy to or from the system's surroundings, then the flow is driven purely by the interchange of kinetic energy (KE) and potential energy (PE). Moreover, the sum of KE and PE is a constant wherever the flow is varying continuously with KE and PE being out of phase at all time. At flow discontinuities such as finite hydraulic jumps, energy is lost according to the first law of thermodynamics. For the variable-density shallow flow and species transport model, the volume per unit width of channel (V), mass per unit width of channel (M), kinetic energy per unit width of channel (KE) and potential energy per unit width of channel (PE) of the liquid–species mixture can be interpreted at any given time as

$$V = \int_0^a h \, \mathrm{d}x, \quad M = \int_0^a \rho h \, \mathrm{d}x, \quad \mathrm{KE} = \int_0^a \frac{1}{2} \rho h u^2 \, \mathrm{d}x \quad \text{and} \quad \mathrm{PE} = \int_0^a \rho g h \left(\frac{h}{2} + z_b \right) \mathrm{d}x \tag{17}$$

where $h = h(x)$, $\rho = \rho(x)$, and $u(x)$ are the total depth, mixture density, and horizontal velocity components defined in the domain $0 \leqslant x \leqslant a$ and $z_b = z_b(x)$ is the bed level above the initial reference datum. If the simulation is accurate, then the volume, mass, and momentum of the system should be conserved at all time provided there is no mass leaving or entering the system and the boundaries are perfectly reflective. The total energy of the system should also be conserved whenever the flow variables are continuous (i.e. without hydraulic jumps or bores).

3. GODUNOV-TYPE FINITE VOLUME SOLVER

A Godunov-type finite volume scheme in conjunction with Roe's approximate Riemann solver is used to solve the variable-density shallow flow and species transport equations on a uniform collocated grid with $\rho h - \rho^{eq} h^{eq}$, $\rho u h$, and $\rho_s c h - \rho_s c^{eq} h^{eq}$ stored at the centre of each cell. For an arbitrary cell i on the grid, the discretized form of (13), omitting tildes for convenience, is

$$\frac{\partial \mathbf{q}}{\partial t}\bigg|_i = \frac{\mathbf{f}_{Wi} - \mathbf{f}_{Ei}}{\Delta x} + \mathbf{h}_i \tag{18}$$

where $\mathbf{f}_{Wi}$ and $\mathbf{f}_{Ei}$ are the corresponding inviscid flux vectors through the west and east sides of the cell and Δx is the cell size. The values of the conserved variables at time $t + \Delta t$ are obtained using a second-order Adams–Bashforth time-stepping method (see e.g. [12]):

$$\mathbf{q}_i^{t+\Delta t} = \mathbf{q}_i^t + \Delta x \left(\frac{3}{2} \frac{\partial \mathbf{q}}{\partial t}\bigg|_i^t - \frac{1}{2} \frac{\partial \mathbf{q}}{\partial t}\bigg|_i^{t-\Delta t} \right) \tag{19}$$

The time step required for a stable solution is determined by the Courant Friedrichs Lewy criterion (CFL), which can be expressed in terms of the Courant number Co. For an arbitrary cell i, the CFL criterion implies

$$\Delta t \leqslant \min \left[\left(\frac{Co \Delta x}{\sqrt{gh} + |u|} \right)_i \right], \quad 0 < Co \leqslant 1 \tag{20}$$

Roe's approximate Riemann solver is used to evaluate the interface fluxes. At each cell edge, Roe's approximate Riemann solver gives

$$\mathbf{f}_i = \tfrac{1}{2}[\mathbf{f}(\mathbf{q}_i^+) + \mathbf{f}(\mathbf{q}_i^-) - |\mathbf{A}|(\mathbf{q}_i^+ - \mathbf{q}_i^-)] \tag{21}$$

in which

$$|\mathbf{A}| = \mathbf{R}|\mathbf{\Lambda}|\mathbf{L} \tag{22}$$

where $\mathbf{q}_i^+$ and $\mathbf{q}_i^-$ are the reconstructed right and left Riemann states of the conserved variables at the cell interface and $\mathbf{A}$ is the flux Jacobian matrix evaluated using the right and left eigenvector matrices $\mathbf{R}$ and $\mathbf{L}$ and the diagonal matrix of the absolute values of the eigenvalues $|\mathbf{\Lambda}|$. For the present system of equations,

$$\mathbf{A} = \begin{bmatrix} 0 & 1 & 0 \\ a^2 - u^2 + \dfrac{(\rho_s - \rho_w)a^2 c}{2\rho_w} & 2u & -\dfrac{(\rho_s - \rho_w)\rho a^2}{2\rho_s \rho_w} \\ -\dfrac{\rho_s u c}{\rho} & \dfrac{\rho_s c}{\rho} & u \end{bmatrix} \tag{23}$$

in which $a = \sqrt{gh}$ is the wave celerity. The eigenvalues of the flux Jacobian matrix are found to be $\lambda_1 = u - a$, $\lambda_2 = u$, and $\lambda_3 = u + a$. The eigenvalues are real and distinct, confirming that the system is strictly hyperbolic. Furthermore, λ_1 and λ_3 define genuinely non-linear fields associated with a shock or rarefaction wave whereas λ_2 defines a linearly degenerate but physically important

field associated with an intermediate contact wave. In matrix form, the absolute values of the eigenvalues are given by

$$|\mathbf{\Lambda}| = \begin{bmatrix} |u-a| & 0 & 0 \\ 0 & |u| & 0 \\ 0 & 0 & |u+a| \end{bmatrix} \tag{24}$$

The left and right eigenvectors of the matrix are:

$$\mathbf{R} = \begin{bmatrix} 1 & \dfrac{(\rho_s-\rho_w)\rho}{\rho_s(\rho_w+\rho)} & 1 \\[3ex] u-a & \dfrac{(\rho_s-\rho_w)\rho u}{\rho_s(\rho_w+\rho)} & u+a \\[3ex] \dfrac{\rho_s c}{\rho} & 1 & \dfrac{\rho_s c}{\rho} \end{bmatrix} \tag{25}$$

and

$$\mathbf{L} = \begin{bmatrix} u+\dfrac{(\rho_w+\rho)a}{2\rho_w} & -1 & -\dfrac{(\rho_s-\rho_w)\rho a}{2\rho_s\rho_w} \\[3ex] -\dfrac{\rho_s c(\rho_w+\rho)a}{2\rho_w\rho} & 0 & \dfrac{(\rho_s-\rho_w)\rho a u}{2\rho_s\rho_w}+\dfrac{(\rho_w+\rho)a}{2\rho_w} \\[3ex] -u+\dfrac{(\rho_w+\rho)a}{2\rho_w} & 1 & -\dfrac{(\rho_s-\rho_w)\rho a}{2\rho_s\rho_w} \end{bmatrix} \tag{26}$$

The model is applicable to constant density shallow flows containing dilute species, i.e. when $\rho = $ constant and $c \neq 0$, and Equation (23) simplifies to give the Jacobian matrix for the conventional shallow water and species advection–diffusion equations.

At each time step, the matrix $|\mathbf{A}|$ is evaluated using averaged values following Roe and Pyke [13], where the Roe averages are

$$u = \frac{u^+\sqrt{(\rho h)^+}+u^-\sqrt{(\rho h)^-}}{\sqrt{(\rho h)^+}+\sqrt{(\rho h)^-}}, \quad c = \frac{c^+\sqrt{(\rho h)^+}+c^-\sqrt{(\rho h)^-}}{\sqrt{(\rho h)^+}+\sqrt{(\rho h)^-}} \quad \text{and} \quad a = \sqrt{\frac{g(h^++h^-)}{2}} \tag{27}$$

A non-linear flux gradient limiter (see [14]) is used to prevent numerical oscillations developing in the solution. The limiter used is minmod, unless otherwise stated.

The source terms (given as components of the vector $\tilde{\mathbf{h}}$) are evaluated at the cell centres using second-order accurate central differences to represent spatial gradients, and are lagged at time t when integrating forward to time $t+\Delta t$. For applications where the source terms could be highly transient, a more accurate treatment is necessary; for example, by upwinding and splitting (see e.g. [15, 16]).

Two types of simple boundary conditions are applied to the cases discussed in this paper, namely transmissive open boundary and reflective closed boundary conditions. At open transmissive boundaries:

$$\rho_0=\rho_1, \quad h_0=h_1, \quad u_0=u_1, \quad \rho_{m+1}=\rho_m, \quad h_{m+1}=h_m \quad \text{and} \quad u_{m+1}=u_m \tag{28a}$$

At closed reflective boundaries:

$$\rho_0 = \rho_1, \quad h_0 = h_1, \quad u_0 = -u_1, \quad \rho_{m+1} = \rho_m, \quad h_{m+1} = h_m \quad \text{and} \quad u_{m+1} = -u_m \qquad (28b)$$

Subscripts 1 and m refer to cells with a boundary interface that lie immediately inside the computational domain. Subscripts 0 and $m+1$ are used to represent the adjacent fictitious cells that lie just outside the domain. These correspond to linear boundary conditions (following [17]). The extension to second order is straightforward, and involves the use of extrapolation for the open boundary case, and an additional ghost cell either end of the domain.

4. RESULTS

The variable-density shallow flow and species transport model was first validated (see [18]) using standard benchmark tests for flows of constant density, where analytical or nearly exact numerical solutions of the shallow water and species transport equations are available. The results presented here are for variable density shallow flows.

4.1. Quiescent equilibrium in a tank with a sinusoidal bed

Ignoring the surface stress, effective stress, and source term in Equations (1)–(3), and noting that $\partial(\rho h)/\partial t$, $\partial(\rho u h)/\partial t$, $\partial(\rho_s c h)/\partial t$, and u are all zero for no flow at steady state, both sides of Equations (1) and (3) reduce to zero, and Equation (2) becomes

$$\frac{\partial(\rho h^2)}{\partial x} = -2\rho h S_{ox} \qquad (29)$$

At steady state, $\rho = \rho(x)$ and $h = h(x)$, and so Equation (29) is essentially an ordinary differential equation. For a horizontal bed ($S_{ox} = 0$), and

$$\rho h^2 = \text{constant} \qquad (30)$$

If the bed is not flat ($S_{ox} \neq 0$), then differentiation of Equation (29) leads to

$$\frac{h}{\rho}\frac{\partial \rho}{\partial x} + 2\frac{\partial h}{\partial x} = -2 S_{ox} \qquad (31)$$

Consider a rectangular tank of length L and sinusoidal bed containing a liquid–species mixture such that Equation (30) is satisfied. If the analytical steady-state (zero flow) solution is input as the initial condition, the system should remain stationary thereafter. The bed topography is chosen as

$$z_b(x) = A\left[1 - \cos\left(\frac{2\pi x}{L}\right)\right] \qquad (32)$$

where x is the horizontal distance along the channel. The variable-density equilibrium solution for the mixture depth and density at steady state is

$$h^{vde}(x) = h_0, \quad \rho^{vde}(x) = \rho_0 \exp\left[\frac{2A}{h_0}\cos\left(\frac{2\pi x}{L}\right)\right] \qquad (33)$$
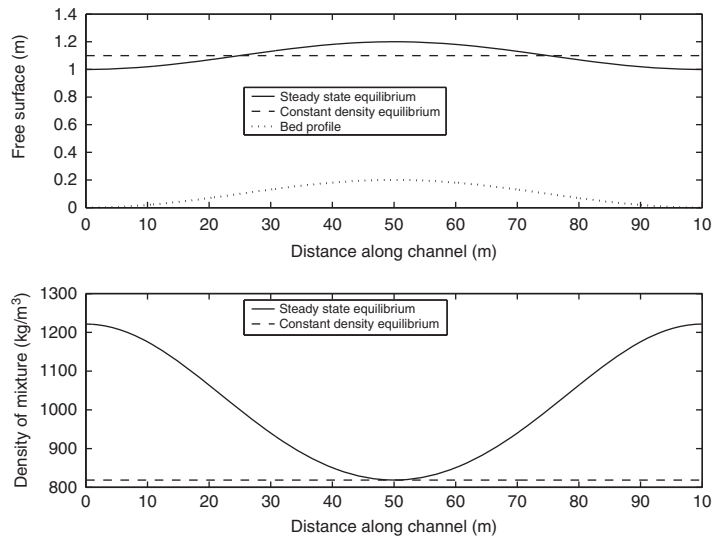
Figure 1. Steady-state variable density and constant density equilibrium solutions for liquid mixture over a sinusoidally varying bed.

In the present case, we choose: $L = 100\,\text{m}$, $A = 0.1\,\text{m}$, $h_0 = 1\,\text{m}$ and $\rho_0 = 1000\,\text{kg/m}^3$. Frictional effects are ignored. The numerical domain is discretized spatially on a uniform grid of 1001 cells (the number selected after grid convergence checks had been undertaken). The time step is $\Delta t = 0.01\,\text{s}$ and the total simulation time is $t = 100\,\text{s}$. The end boundary conditions are reflective. Figure 1 shows the bed profile (dotted line), and the steady-state variable-density equilibrium predictions of the free surface (solid line) and the density distribution (solid line). The constant density equilibrium depth and density distributions, $h^{\text{eq}} = h_s$ and $\rho^{\text{eq}} = \rho_w$, are also plotted for comparison purposes. Non-dimensional depth, velocity and density errors were also estimated by calculating $h^* = (h - h^{vde})/h^{vde}|_{\max}$, $u^* = u/\sqrt{gh^{vde}}|_{\max}$ and $\rho^* = (\rho - \rho^{vde})/\rho^{vde}|_{\max}$ at the first, middle and last cells along the channel, and were found to be invariably less than 10^{-6}. The error in the density was slightly divergent with time, but remained below 10^{-8}. The non-zero errors arise from the half time-step lag in the treatment of the source terms. This partly indicates that the simple approach taken to handling the source terms is adequate for an engineering calculation.

4.2. 1-D density dam break with a single initial discontinuity

This case considers the perturbation effect caused by two adjacent liquids of different densities but equal initial depth. The physical domain consists of a horizontal channel of length $L = 500\,\text{m}$ separated into two equal sections by an infinitesimally thin wall. The liquid to the left of the wall has density $\rho_L = 10\,\text{kg/m}^3$, whereas the liquid to the right has density $\rho_R = 1\,\text{kg/m}^3$. The two liquid regions are initially at rest and both have uniform depth of $h_0 = 1\,\text{m}$. The acceleration due to gravity is $g = 1\,\text{m/s}^2$. Frictional effects are neglected. The grid is uniform with 5000 cells, and the time step is $\Delta t = 0.02\,\text{s}$. The wall is suddenly removed at time $t = 0\,\text{s}$. Figure 2 illustrates the stacked $x - t$ plots showing time evolution of the depth, velocity and concentration from $t = 0$ to
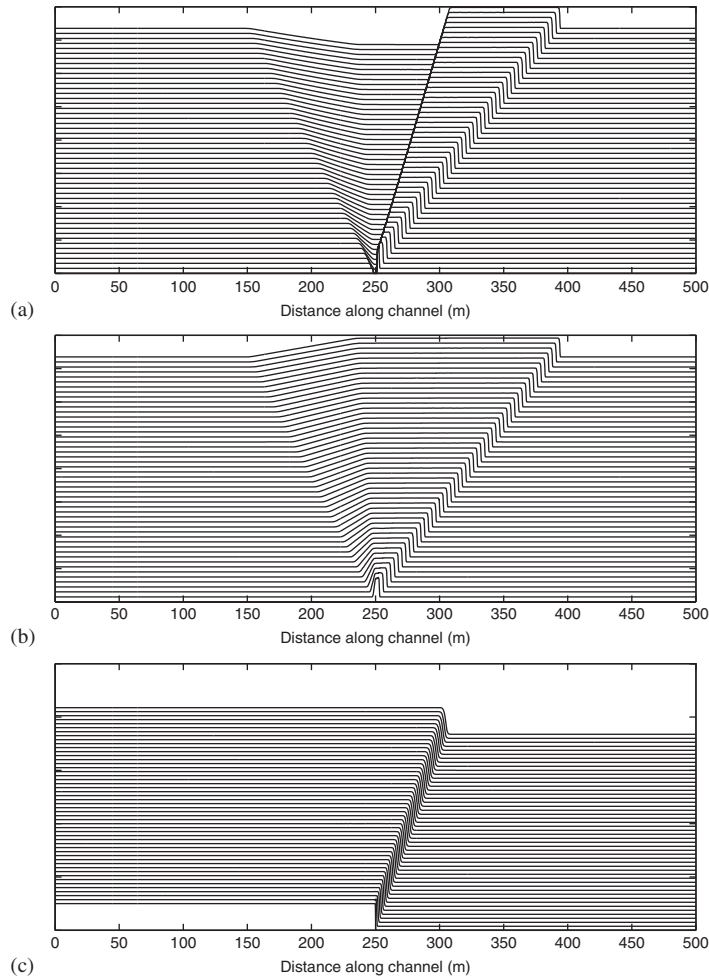
Figure 2. Density dam-break test with a single initial discontinuity: stacked $x-t$ plots of the depth, velocity and concentration for $t \leqslant 100$ s. (a) Free surface elevation; (b) depth-averaged velocity; and (c) species concentration.

100 s. In Figure 2, as time increases, each successive profile is shifted vertically relative to the previous profile (the other $x-t$ plots given in the paper are obtained by the same method). Initially the hydrostatic pressure difference at the interface of the two liquids drives a flow of higher density liquid towards the right, pushing the lower density liquid ahead. To conserve mass, the free surface of the lower density liquid rises and a rightward propagating shock-like bore forms (Figure 2(a)). This is evident also as a step change in velocity (Figure 2(b)). The bore occurs entirely in the less dense liquid, and so there is no trace of it in the concentration plot (Figure 2(c)). As can be seen in the free surface elevation $x-t$ plot, there is a moving contact surface behind the bore, where the liquid depth drops suddenly as the contact wave passes. This contact surface marks the boundary between the two liquids that were either side of the interface initially, and is where the

concentration jumps discontinuously. As diffusion is neglected, the two liquids are permanently separated by the moving contact surface. The contact surface propagates to the right in the depth and concentration $x-t$ plots, but is not visible on the depth-averaged velocity either side of the shear wave. A leftward propagating expansion-type wave is evident in Figure 2(a), located entirely in the denser liquid. The expansion-type wave fans out with time, smoothing out the depth changes in the region of denser liquid. There is, however, no sign of this wave in the concentration plot (Figure 2(c)). From Figure 2(a) it can be discerned that the bore travels to the right at 1.43 m/s, the contact wave to the right at 0.578 m/s and the expansion wave to the left at 1 m/s. The bore speed is in approximate agreement with the wave celerity $u_b = \sqrt{gh_b} = \sqrt{1.63} = 1.28$ m/s obtained using the predicted mixture depth. The flow velocities before and after the bore passes are zero and 0.567 m/s, respectively.

The mechanisms of the density dam break are similar to that of a dam break induced by change in free surface depth, in that a leftward rarefaction, a rightward shock and a contact wave are formed. Toro [17] gives details of the different types of waves, and the related solutions of the Riemann problem. Similar wave structures occur in shock tube gas dynamics (see e.g. [19]).

4.3. Symmetric 1-D density dam break with two initial discontinuities

The following parameter study investigates the effect of a region of different density within a long channel of horizontal bed containing otherwise uniform density material of initially uniform depth, as illustrated in Figure 3. At the left-hand side and right-hand side of the channel, the liquid is of density ρ_1. At the centre of the channel there is a liquid column of density ρ_2 and width w. In these parameter tests: $L = 100$ m; $h = 1$ m; $w = 1$ m; $\rho_1 = 1$ kg/m^3; $\rho_2 = 0.1, 0.5, 0.9, 1, 1.1, 1.5$, 10, and 100 kg/m^3; and $g = 1$ m/s^2. Frictional effects are ignored.

A simple physical interpretation of the liquid behaviour is as follows. The central liquid column falls or rises to an equilibrium level depending on whether the density ratio ρ_2/ρ_1 is, respectively, greater than or less than unity. At equilibrium there is a balance between the hydrostatic pressure thrusts produced by the different liquids either side of the density interface. On being released, the system tries to restore the region of density ρ_2 to an equilibrium depth h_2 with an equilibrium width w_2. Once equilibrium is established, the region of density ρ_1 has a new equilibrium depth h_1. With reference to Figure 3, the hydrostatic balance of pressure thrusts implies

$$\rho_1 g h_1^2 = \rho_2 g h_2^2 \tag{34}$$

Thus, by rearrangement,

$$h_2 = h_1 \sqrt{\frac{\rho_1}{\rho_2}} \tag{35}$$

Provided that the domain length L is sufficiently large, $h_1 \approx h$, and so an approximation for h_2 can be obtained from Equation (35). The equilibrium width, w_2, of the central liquid column of density ρ_2 can then be estimated from volume (area in 1-D) conservation to be

$$w_2 = w \frac{h}{h_2} \tag{36}$$

The equilibrium depth h_2 and width w_2 are independent of L.

The computational domain is uniformly discretized in space with $\Delta x = 0.05$ m and the time step is $\Delta t = 0.01$ s. These values were determined by grid convergence and CFL stability tests
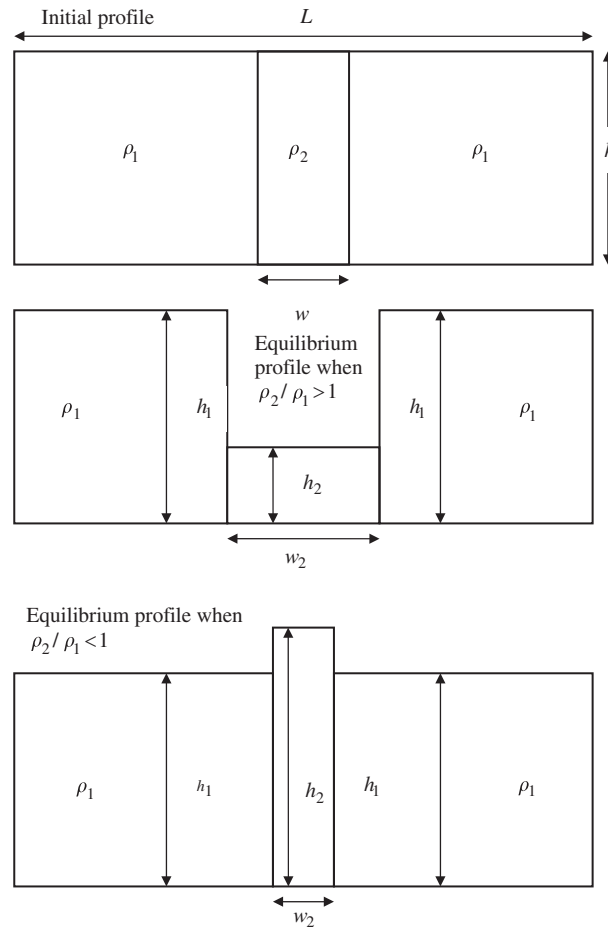
Figure 3. Density dam-break tests with two initial discontinuities: initial and
equilibrium states of the system.

(see Appendix A). The length L is chosen sufficiently large compared with w_2 so that volume conservation approximately holds. The domain length is selected to be sufficiently long that the equilibrium width is achieved before reflected waves disturb the solution in the central region.

Case DB1: $\rho_2 = 0.1\,\mathrm{kg/m^3}$. In this case, the liquid in the central region is a factor of 10 times less dense than the liquid in the regions either side. As a result, the denser liquid moves inwards towards the centre of the domain, squeezing the less dense region upwards. The analytical equilibrium dimensions of the central region are $h_2 \approx 3.16\,\mathrm{m}$ and $w_2 \approx 0.316\,\mathrm{m}$. Figure 4 displays the depth and velocity profiles at times $t = 2$ and $30\,\mathrm{s}$, respectively. The initial density difference at the liquid interface produces a pair of rarefaction waves propagating outwards and a pair of shock-like bores propagating inwards. The bores collide at the centre, creating a clapotis-type sudden rise in the free surface elevation to a value corresponding to the analytical equilibrium solution, by $t = 1\,\mathrm{s}$. After this, the central column of less dense liquid remains almost unchanged
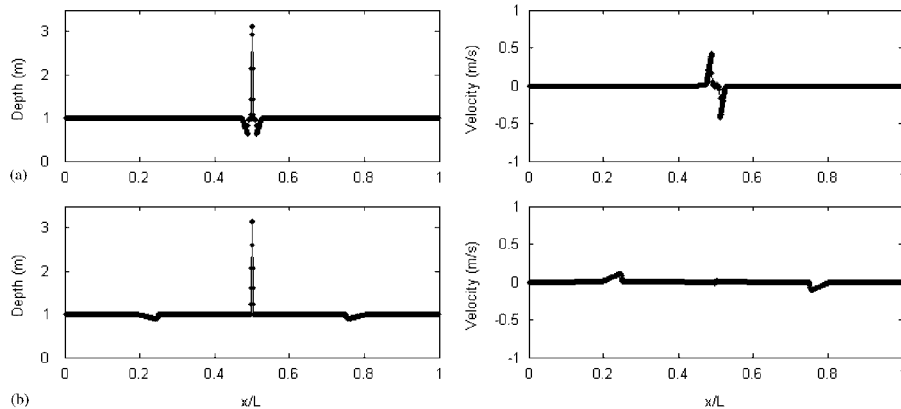
Figure 4. Density dam break: two initial discontinuities: $\rho_2 = 0.1\,\text{kg/m}^3$. Flow depth and velocity profiles at (a) $t = 2$ and (b) $t = 30\,\text{s}$.

in profile. The rarefaction waves progressively move outwards, but with decreasing velocity. Elsewhere the liquid is almost stationary. Figure 5 presents stacked $x - t$ plots showing the behaviour of the depth, velocity and concentration profiles along the channel from $t = 0$ to $50\,\text{s}$. Outward propagating rarefaction waves are initially released from the density interfaces. Meanwhile, two shock-type bores travel inwards and are reflected at the centre causing the lower density liquid region to contract and almost immediately establish its equilibrium shape (i.e. at about $t = 1\,\text{s}$). The contact surfaces between the low- and high-density liquid regions remain more or less steady thereafter. With time, the rarefaction waves continue to travel outwards decreasing in strength and speed.

Cases DB2 and DB3: $\rho_2 = 0.5\,\text{kg/m}^3$ and $\rho_2 = 0.9\,\text{kg/m}^3$. Simulations were also undertaken for densities $\rho_2 = 0.5\,\text{kg/m}^3$ and $\rho_2 = 0.9\,\text{kg/m}^3$. The results were similar to those for $\rho_2 = 0.1\,\text{kg/m}^3$, with almost identical wave speeds (being mainly dependent on the liquid depth) but much reduced amplitude with regard to free surface disturbance and flow velocity. Figure 6 shows a typical set of results obtained for $\rho_2 = 0.5\,\text{kg/m}^3$ at $t = 30\,\text{s}$, which are very similar in form, though much lower amplitude, than obtained for $\rho_2 = 0.1\,\text{kg/m}^3$ at $t = 30\,\text{s}$ (Figure 4(b)). The stacked $x - t$ plots are not presented for $\rho_2 = 0.5\,\text{kg/m}^3$ and $\rho_2 = 0.9\,\text{kg/m}^3$ as they are very similar in form to that for $\rho_2 = 0.1\,\text{kg/m}^3$.

Case DB4: $\rho_2 = 1\,\text{kg/m}^3$. In this special case the liquid density is the same throughout the channel. No results are presented here because the system remains stationary in the absence of any perturbation.

Case DB5 and DB6: $\rho_2 = 1.1\,\text{kg/m}^3$ and $\rho_2 = 2.0\,\text{kg/m}^3$. The flow patterns obtained for relative density $0 > \rho_2/\rho_1 > 10$ have common features. Again the wave speeds are almost the same; the relative density merely affects the amplitude of the free surface motions. Figure 7 shows the depth and velocity profile along the channel at $t = 30\,\text{s}$ for $\rho_2 = 2.0\,\text{kg/m}^3$. The form is strikingly similar to the equivalent plot for $\rho_2 = 10\,\text{kg/m}^3$, for which a detailed discussion is given below.

Case DB7: $\rho_2 = 10\,\text{kg/m}^3$. In this case, the liquid in the central region is a factor of 10 denser than the liquid either side of the interfaces. The density differences cause liquid motions to occur. The equilibrium depth and width of the central region are estimated from Equations (35) and
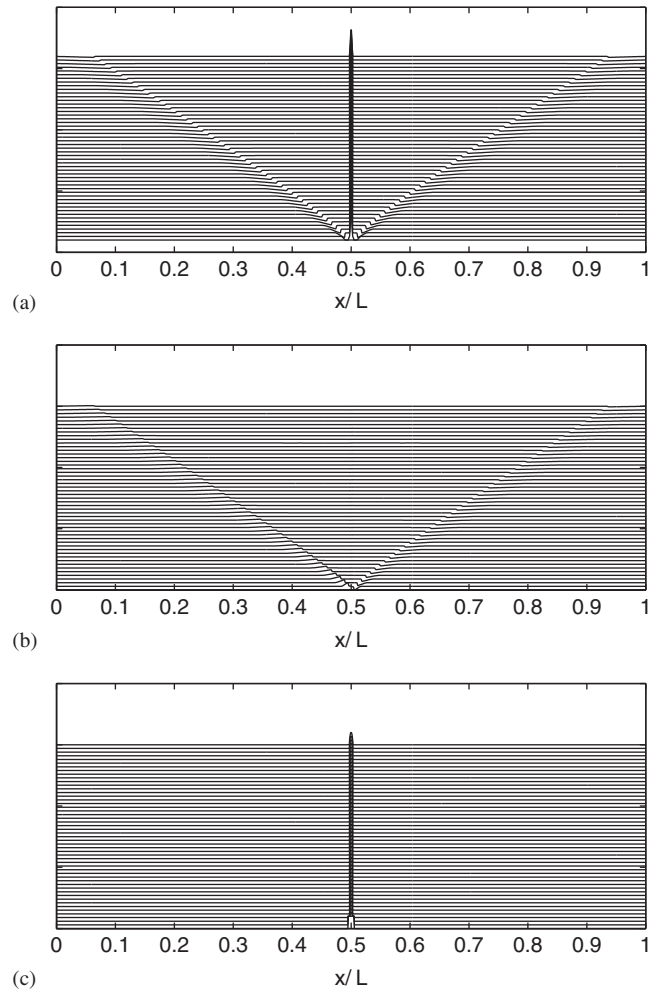
Figure 5. Density dam break: two initial discontinuities: $\rho_2 = 0.1\,\text{kg/m}^3$. Stacked $x - t$ plots of the depth, velocity and concentration for $t \leqslant 0\,\text{s}$. (a) Free surface elevation; (b) depth-averaged velocity; and (c) species concentration.

(36) to be $h_2 \approx 0.316\,\text{m}$ and $w_2 \approx 3.162\,\text{m}$. Figure 8 displays the depth and velocity profiles at times $t = 1$, 4, 12, and 30 s, respectively. Initially, the central column of higher-density liquid falls under gravity, driving left and right shock-type bores into the adjacent lower-density liquid regions, followed by rarefaction waves travelling in opposite directions. By time $t = 1\,\text{s}$ (Figure 8(a)), the initial inward propagating rarefaction waves have already reflected at the centre of the channel where the liquid-free surface is at its lowest level. Reflected rarefaction waves also cause the free surface of the central column to fall rapidly to about half its initial depth. The leading shock-type bores then continue to travel outwards with almost vertical front faces. The fronts of the bores travel fastest with liquid behind travelling more and more slowly as the free surface level reduces.
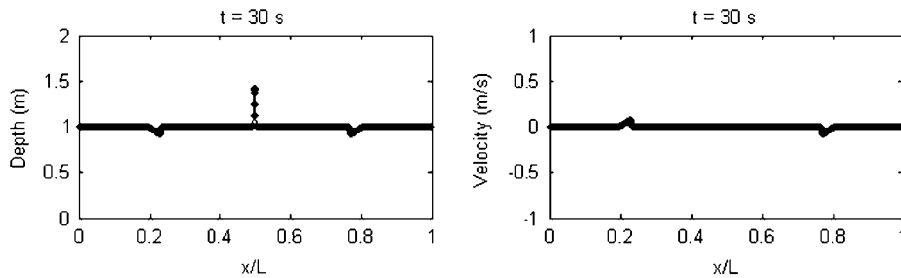
Figure 6. Density dam break: two initial discontinuities: $\rho_2 = 0.5\,\text{kg/m}^3$. Flow depth and velocity profiles at $t = 30\,\text{s}$.
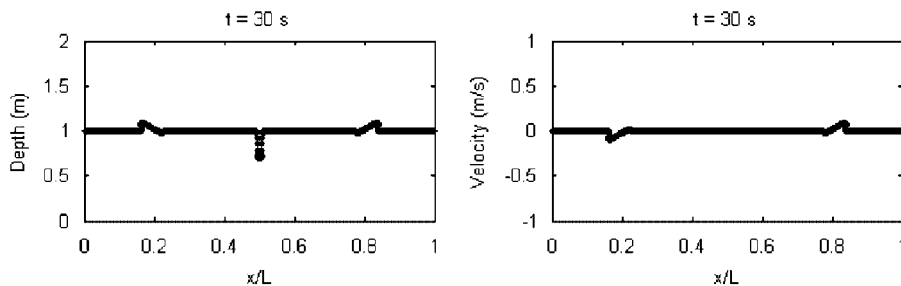

Figure 7. Density dam break: two initial discontinuities: $\rho_2 = 2.0\,\text{kg/m}^3$. Flow depth and velocity profiles at $t = 30\,\text{s}$.

Meanwhile, the central column of denser liquid continues to fall and spread out under gravity. By $t = 4\,\text{s}$ (Figure 8(b)), a zone of still liquid can be seen, as the denser liquid bottoms out. At this stage, the denser liquid has spread out too far in a similar manner to an over-expanded compressible flow. At $t = 12\,\text{s}$ (Figure 8(c)), the denser liquid at the centre of the domain has started to readjust for the over-spreading. The depth profile at the centre has risen by a small amount since $t = 4\,\text{s}$ and has become more rectangular in shape while slightly contracting. By $t = 18\,\text{s}$, the central rectangular depth profile has almost become established. The adjustment for over-spreading has ceased, releasing a further pair of small bores into a depression region behind the main bores. At $t = 30\,\text{s}$ (Figure 8(d)), the height of the shock-type bore front has reduced, as the liquid making up the bore has to cover an increasing distance along the channel. The decrease in height is accompanied with a reduction in bore speed. The second pair of bores follows behind, propagating in the outwards directions. Thus, the leading disturbance in both directions is a classical N-wave. By $t = 50\,\text{s}$, the depth and the width of the central column reach steady-state values of 0.315 and 3.1 m, respectively. Figure 9 gives the stacked $x-t$ plots showing evolution of the depth, velocity and concentration profiles along the channel from $t = 0$ to $t = 50\,\text{s}$ plotted at $1-\text{s}$ intervals. The sudden collapse of the denser liquid in the central column causes primary shock waves to be created and propagate as bores in the direction from high to low density. Two outward propagating bores are generated, travelling in opposite directions. Each primary bore decreases in strength with time, which can be seen from the curved shock path. Meanwhile, a pair of rarefaction waves travels inward from the interfaces. The rarefaction waves are almost immediately reflected at the
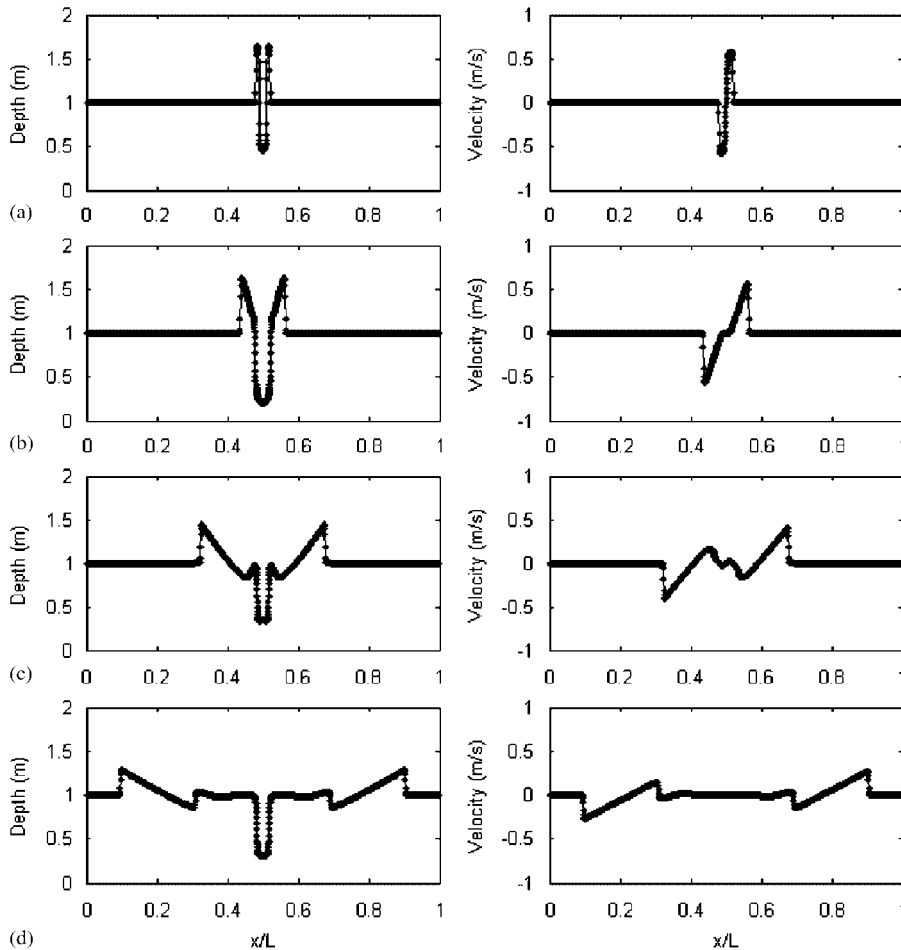
Figure 8. Density dam break: two initial discontinuities: $\rho_2 = 10\,\mathrm{kg/m^3}$. Flow depth and velocity profiles at (a) $t = 1\,\mathrm{s}$; (b) $t = 4\,\mathrm{s}$; (c) $t = 12\,\mathrm{s}$; and (d) $t = 30\,\mathrm{s}$.

centre, and then move outward, weakening rapidly. Two contact waves are also clearly evident at the interfaces between the higher- and lower-density liquids. These confirm that over-expansion occurs during the first 2 s. The width of the denser region then contracts, until a minimum width occurs at about $t = 10\,\mathrm{s}$ when two outward-directed secondary bores are released. Afterwards, the contact waves at the interface between the regions of different density become stationary, and the primary and secondary bores continue to travel outward. The primary bore travels in a curved path on the $x - t$ plane as it loses height and speed.

Case DB8: $\rho_2 = 100\,\mathrm{kg/m^3}$. In this case, the liquid in the central region is one hundred times denser than the liquid either side. The analytical equilibrium depth and width of the central region are $h_2 = 0.1\,\mathrm{m}$ and $w_2 = 10\,\mathrm{m}$, respectively. It should be noted that the time taken for the system to reach equilibrium is much greater than that of the previous case because of the bigger density difference of the two fluids. Figure 10 displays the depth and velocity profiles at times $t = 18$, 108,
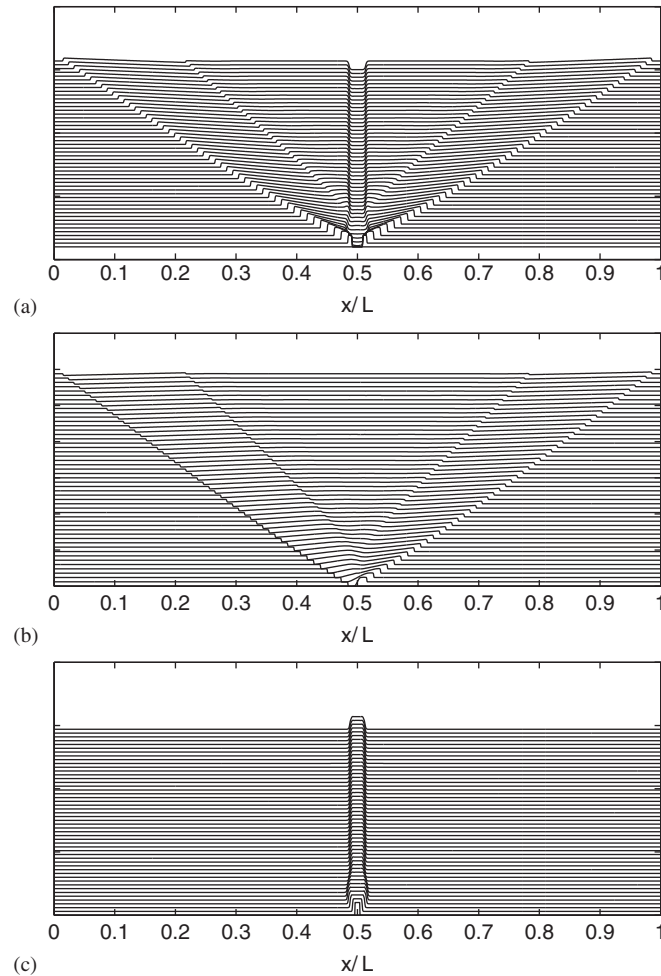
Figure 9. Density dam break: two initial discontinuities: $\rho_2 = 10\,\text{kg/m}^3$. Stacked $x-t$ plots of the depth, velocity and concentration for $t \leqslant 50\,\text{s}$. (a) Free surface elevation; (b) depth-averaged velocity; and (c) species concentration.

and 180 s, respectively. At first, the hydrostatic pressure differences at the interfaces between the two liquids drive two shock-type bores outwards into the adjacent lower-density liquid regions. Rarefaction waves travelling inwards are reflected at the centre, causing the central column to fall rapidly, its free surface almost touching bed level at $t = 18\,\text{s}$ (Figure 10(a)). Meanwhile, the width of the central column increases as the depth decreases in order to conserve mass. The fronts of the bores travel fastest, with liquid behind travelling more and more slowly as the free surface level reduces. At this stage, the denser liquid has spread far outwards as a result of the over-expanded flow. By $t = 108\,\text{s}$ (Figure 10(b)), a zone of still liquid begins to grow near the centre. The denser liquid region has become more rectangular in shape and contracted slightly. The adjustment for over-spreading releases a further pair of small bores into a depression region
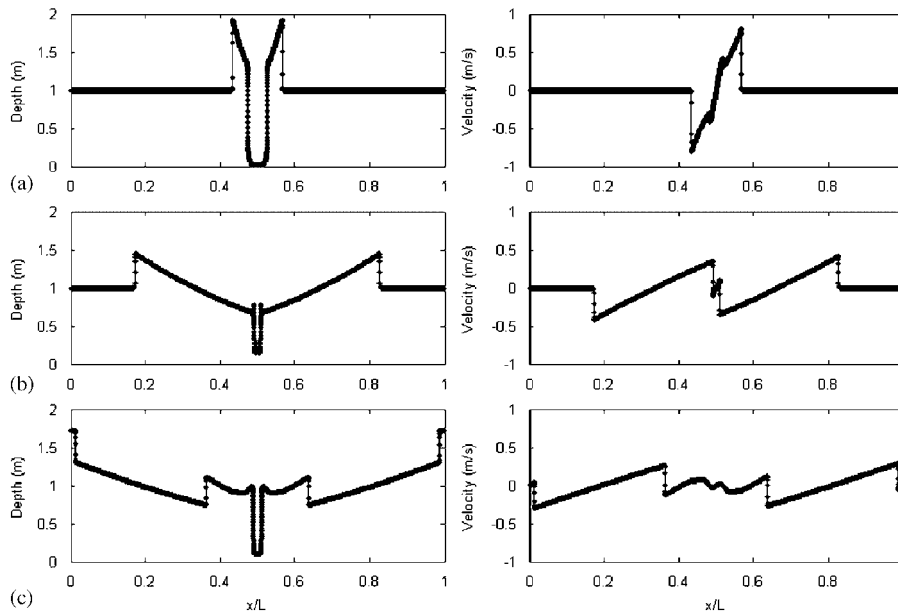
Figure 10. Density dam break: two initial discontinuities: $\rho_2 = 100\,\mathrm{kg/m}^3$. Flow depth and velocity profiles at (a) $t = 18\,\mathrm{s}$; (b) $t = 108\,\mathrm{s}$; and (c) $t = 180\,\mathrm{s}$.

behind the main bores. At $t = 180\,\mathrm{s}$ (Figure 10(c)), the central denser liquid has a nearly rectangular (and unchanging) depth profile, corresponding to the equilibrium condition. The primary and secondary bores continue to travel outwards from the centre, losing height and speed as liquid is redistributed along the channel. From Figure 11 it can be observed that the convergence rate of the free surface elevation at the centre of the channel is much slower than that of the previous case. The numerically predicted width and depth of the denser liquid region undergo damped oscillations as they tend to equilibrium at about $t = 300\,\mathrm{s}$. Figure 12 illustrates the evolution of the depth, velocity and concentration profiles along the channel until $t = 300\,\mathrm{s}$. Three pairs of outward propagating shock-type bores can be observed in the depth and velocity plots. The primary pair of bores is created by liquid density differences. Secondary and tertiary pairs of shock waves are released from the edges of the denser liquid region each time it starts to readjust for over-expansion and under-expansion of its width.

5. CONCLUSIONS

This paper has presented a mathematical formulation of the 1-D non-linear shallow flow and species transport equations designed for variable density horizontal free-surface flows. The formulation deals with cases where the density difference in different flow regions is sufficiently large as to drive flows. It is assumed that the liquid–species mixture is instantaneously fully mixed in the vertical direction, but can vary in the horizontal plane. A Godunov-type finite volume numerical scheme has been used to solve the variable-density non-linear shallow flow equations in order to permit steep fronts to be modelled. The hyperbolic conservation laws have been transformed into an
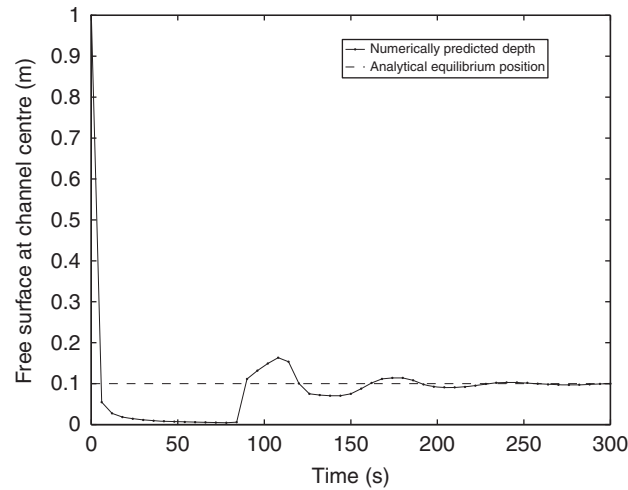
Figure 11. Density dam break: two initial discontinuities: $\rho_2 = 100\,\mathrm{kg/m^3}$. Time history of free surface elevation at the channel centre.

equilibrium-corrected form that balances the flux gradient and source terms using the generalized balancing technique derived by Rogers *et al.* [11]. For the cases considered, it was sufficient to subtract the constant density equilibrium solution when setting up the deviatoric equation system in the numerical solver.

Using the full 1-D variable-density non-linear shallow flow and species transport equations, analytical steady-state solutions were derived for certain idealized cases that were used to help validate the numerical solver. Predictions of the steady-state depth and density distributions along a channel for a variable-density liquid–species mixture, where the bed was sinusoidal, were in almost exact agreement with the analytical solutions. Further predictions were made for variable-density cases analogous to 1-D dam breaks, where the flow was driven by initial discontinuities in density. The numerical predictions in these cases converged to equilibrium values in agreement with approximate analytical solutions based on mass conservation.

The first parameter study investigated the transient flow features that occur for two adjacent liquids of different densities but the same initial depth in a rectangular tank. It was observed that a shock-type bore propagated from the initial interface between the two liquids into the lower density liquid (which corresponded to the lower initial ρh^2 value). A contact wave followed the bore, while a rarefaction wave propagated simultaneously in the opposite direction into the higher-density liquid. The wave structures from this test were found to be similar to those that occur in shock tube gas dynamics.

The second parameter study considered the motions induced by an initial liquid column of different density than surrounding ambient liquid. The initial depth was the same everywhere in the tank, and therefore the ρh^2 value depended solely on the density. The liquid motions were characterized according to whether the column had higher, the same or lower density than the surrounding liquid. For the case where the density of the column was higher than that of the surrounding liquid, the transient flow behaviour was similar to that of a conventional wet-bed dam break. Bores propagated from the density interface into the low-density surrounding liquid
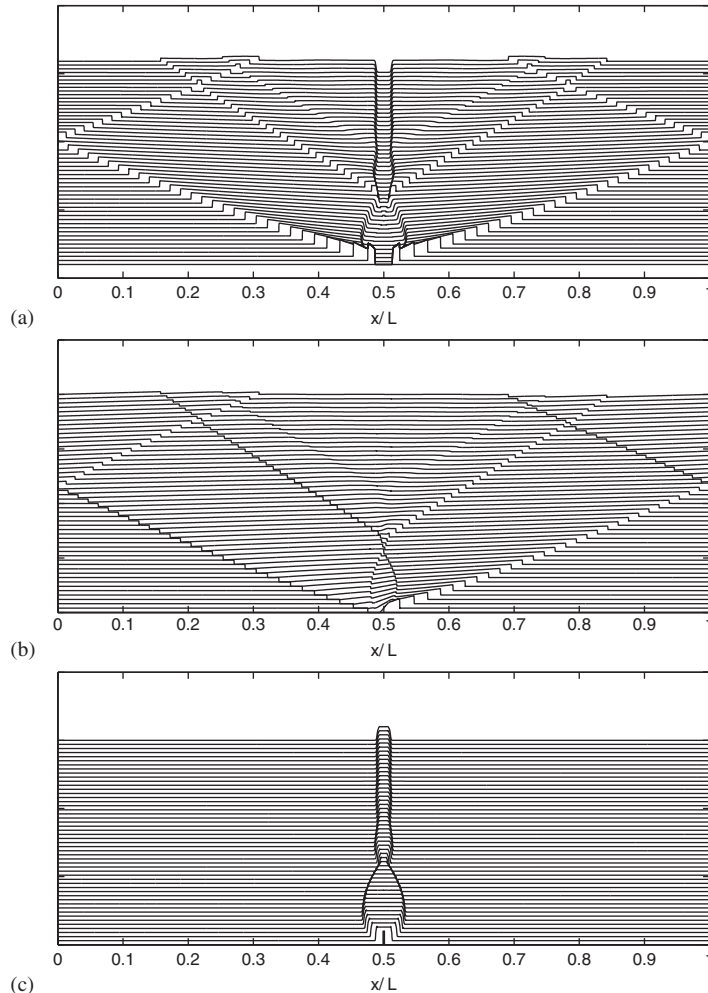
Figure 12. Density dam break: two initial discontinuities: $\rho_2 = 100\,\text{kg/m}^3$. Stacked $x-t$ plots of the depth, velocity and concentration for $t \leqslant 300\,\text{s}$. (a) Free surface elevation; (b) depth-averaged velocity; and (c) species concentration.

as rarefaction waves propagated in the opposite direction into the high-density liquid of the central column. Reflection of the rarefaction waves caused a sudden drop in free surface elevation at the centre. In establishing equilibrium, the high-density central region underwent a series of readjustments counteracting overshoots in the free surface motions. When the density was the same either side of the interface, the system remained stationary, as would be expected. For the case where the density was lower inside than that outside of the column, bores initiated from the interface propagated inwards into the low-density region while rarefactions propagated outwards. At equilibrium, a peak formed at the centre of the tank due to the superposition of the inward propagating bores.

The model should be applicable to a wide class of environmental free surface flows, including hyper-concentrated sediment-laden flows in rivers, and debris flows.

APPENDIX A

Figure A1 shows a typical set of flow depth and velocity profiles along the channel obtained for the symmetric 1-D density dam break with two initial discontinuities, Case DB7: $\rho_2 = 10\,\text{kg/m}^3$), using grids of 100, 200, 500, and 2000 cells. The coarser grids lack sufficient resolution to model the sharp changes that take place at bore fronts. The results obtained for the 500 and 2000 cell grids are very similar, indicating that grid convergence is achieved by 2000 cell grid. In all simulations
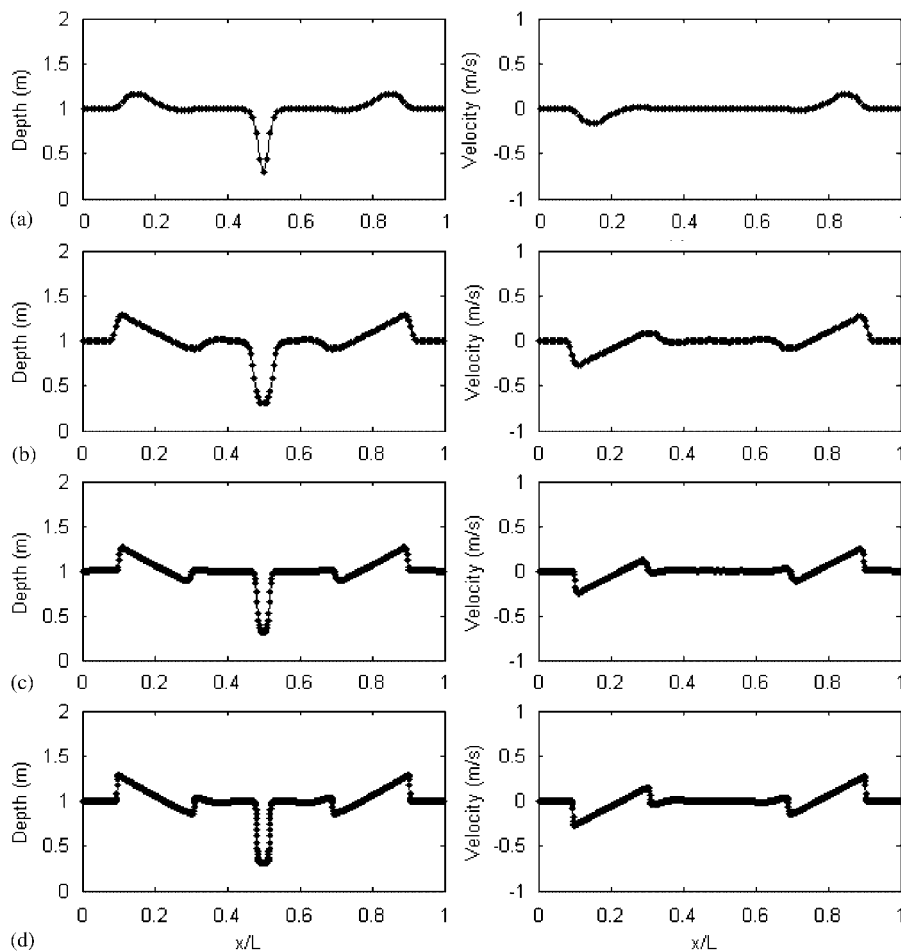

Figure A1. Density dam break: two initial discontinuities: $\rho_2 = 10\,\text{kg/m}^3$. Flow depth and velocity profiles at $t = 30\,\text{s}$ using grid of (a) 100 cells; (b) 200 cells; (c) 500 cells; and (d) 2000 cells.

presented herein for the symmetric 1-D density dam break with two initial discontinuities, $\Delta x = 0.05$ m $\Delta t = 0.01$ s, corresponding to Courant numbers in the range from 0.1 to 0.5.

ACKNOWLEDGEMENTS

REFERENCES

1. Hutter K, Svendsen B, Rickenmann D. Debris flow modelling: a review. *Continuum Mechanics and Thermodynamics* 1996; **8**:1–35.
2. Zhang KF, Dong P. Computer code for simulating hyper-concentrated sediment motions in steady and unsteady flows. *Applied Mathematical Modelling* 2000; **24**(7):495–510.
3. Fraccarollo L, Papa M. Numerical simulation of real debris-flow events. *Journal of Physics and Chemistry of the Earth*, *Part B* 2000; **25**(9):757–763.
4. Liang Q, Borthwick AGL, Taylor PH, Huang J. Godunov-type quadtree model of species dispersion in shallow flows. In *Shallow Flows*, Jirka GH, Uijttewaal WSJ (eds). A.A. Balkema Publishers: The Netherlands, 2004; 439–447.
5. Sommeijer BP, van Der Houwen PJ. Parallel solution of a coupled flow and transport model for shallow water. *International Journal for Numerical Methods in Fluids* 2002; **38**:849–859.
6. Murillo J, Burguete J, Brufau P, García-Navarro P. Coupling between shallow water and solute flow equations: analysis and management of source terms in 2D. *International Journal for Numerical Methods in Fluids* 2005; **49**(3):267–299.
7. Cao Z, Pender G, Wallis S, Carling P. Computational dam-break hydraulics over erodible sediment bed. *ASCE Journal of Hydraulic Engineering* 2004; **130**(7):689–703.
8. Cao Z, Pender G, Carling P. Shallow water hydrodynamic models for hyperconcentrated sediment-laden floods over erodible bed. *Advances in Water Resources* 2006; **29**(4):546–557.
9. Takahashi T. *Debris Flow*: *Mechanics*, *Prediction and Countermeasures*. Taylor & Francis: London, 2007.
10. Abbott MB. *Computational Hydraulics*. Pitman Advanced Publishing Program: London, 1979.
11. Rogers BD, Borthwick AGL, Taylor PH. Mathematical balancing of flux gradient and source terms prior to using Roe's approximate Riemann solver. *Journal of Computational Physics* 2003; **192**(2):422–451.
12. Canuto C, Hussaini MY, Quarteroni A, Zang TA. *Spectral Methods in Fluid Dynamics*. Springer: Berlin, 1988.
13. Roe PL, Pyke J. Efficient construction and utilisation of approximate Riemann solutions. *Computer Methods in Applied Science and Engineering*. North-Holland: Amsterdam, 1984.
14. Hirsch C. *Numerical Computation of Internal and External Flows*. Wiley: New York, 1990.
15. Goutal N, Maurel F. A finite volume solver for 1D shallow-water equations applied to an actual river. *International Journal for Numerical Methods in Fluids* 2002; **38**(1):1–19.
16. Guinot V. *Godunov-type Schemes*: *An Introduction for Engineers*. Elsevier Science B.V.: Amsterdam, 2003.
17. Toro EF. *Shock-capturing Methods for Free-surface Shallow Flows*. Wiley: Chichester, 2001.
18. Leighton FZ. Numerical modelling of shallow flows with horizontal density variation. *D.Phil. Thesis*, University of Oxford, U.K., 2005.
19. Liepmann HW, Roshko A. *Elements of Gas Dynamics*. Wiley: New York, 1957.